Effects of interface roughness on cohesive strength of self-assembled monolayers

Chen Zhang [a], Amnaya P. Awasthi [c], Philippe H. Geubelle [a,*], Martha E. Grady [b],
Nancy R. Sottos [b]

[a] *Department of Aerospace Engineering, University of Illinois at Urbana-Champaign, IL 61801, USA*
[b] *Department of Materials Science and Engineering, University of Illinois at Urbana-Champaign, IL 61801, USA*
[c] *Department of Mechanical and Aerospace Engineering, University of Florida, Gainesville, 32611, USA*

A B S T R A C T

Self-assembled monolayers (SAMs) are aggregates of small molecular chains that have the property to form highly ordered assemblies. The choice of terminal groups on the chains makes them excellent contenders of molecular-level tailoring. Molecular dynamics (MD) simulations and experimental observations of spallation of two SAM-enhanced gold-film/silicon-substrate interfaces have shown that the cohesive strength of SAM-enriched transfer-printed interfaces is strongly dependent on the choice of terminal groups. Though the MD results of perfectly ordered atomistic surfaces show the same qualitative trend as the experiments, they over-predict the interfacial cohesive strengths by a factor of about 50. Results from AFM studies have revealed that the roughness of these interfaces is of the same order (~1 nm) as the range of atomistic interactions. Hence, surface roughness is a key contributor in significantly reducing interfacial cohesive strength in these systems. In this manuscript, a continuum-level study is performed to investigate the influence of surface roughness on the cohesive strength of the interface between a Si/SAM substrate and a transfer-printed gold film. We approximate the film as a deformable continuum interacting with a rough substrate of SAMs represented by a harmonic function. Using a cohesive law derived from MD, spallation is simulated to evaluate the effective traction-separation characteristics for the rough SAM–gold interface. Our analysis shows that incorporating roughness may reduce the interfacial cohesive strength by an order of magnitude depending on the film properties and the surface roughness. Additionally, we observe that the gold film adopts unique separation attributes based on roughness parameters and material properties.

© 2016 Elsevier B.V. All rights reserved.

1. Introduction

Self-assembled monolayers (SAMs) are aggregates of small molecular chains formed spontaneously by chemical adsorption of an active surfactant in an organic solvent on a solid substrate. The monolayers are usually closely packed and have a highly ordered structure. SAMs consist of three building blocks: a head functional group that has strong affinity to the substrate, a tail function group that establishes the outer layer of the film and a short nanometer-range hydrocarbon chain that connects the head and tail groups. Examples of this formation include the widely used alkanethiol chains on gold surfaces [1,2]. A large number of attractive features can be achieved by using SAMs with different functional groups, especially for applications associated with molecular ordering, growth, wetting, adhesion, lubrication and corrosion [3].

The interfacial properties of SAM-enhanced systems have stimulated extensive research in the recent past. Chemical abilities of SAM terminal groups were studied and examined to produce biocompatible interfaces [4,5]. In these studies, synthetic interfaces with possible extensions and spreading of biological cells in different directions based on chosen SAM functional groups were produced and examined. Losego et al. [6] looked at the effects of chemical bonding on heat transport across SAM interfaces. They found that the nature of bonding between SAMs and adjacent solid layers has a major effect on the heat conductance of SAM system. In a later study, Tian et al. [7] examined the SAM-enhanced solid–liquid interface and showed that a stronger bonding in the SAM-system causes an improved thermal transport across the solid–liquid interface. Researchers have also studied SAMs for interfacial electrical transport to substrate through different functional groups [8,9].

The focus of this manuscript is to evaluate the mechanical properties of SAM-enhanced film/substrate interfaces. Related studies include the work of Bush et al. [10], who measured the elastic modulus, work of adhesion and interfacial shear strength of methyl-terminated alkylsilane SAMs through scanning probe normal and lateral force measurements. Houston and coworkers [11–13] measured differences in frictional behavior of alkanethiol monolayers due to different end group chemistries and chain lengths. Liechti et al. [14] developed a high-vacuum facility to study the interfacial toughness between silicon surfaces and carboxyl/diamine terminated SAMs, and compared their different behavior under vacuum and ambient conditions. Li et al. [15] examined the adhesion, friction and water contact angle of SAM-modified titanium substrate. Owing to the small size and structured feature of SAMs, molecular dynamics (MD) simulations have also been used to study the interfacial mechanical properties of SAM-modified interfaces. Gerdy and Goddard predicted the structure and tilt angles of SAMs of alkanethiols on gold [16]. Zhang et al. [17] performed *ab initio* quantum chemical calculations of alkanethiols on Au(111) and used the force field to perform MD simulations to study the superlattice structures of alkanethiol SAMs on Au(111) for various chain lengths over a range of temperatures. Wu et al. [18] examined the sliding friction behavior of SAM under non-flat contact. Fang et al. [19] modeled nanoindentation of SAM-enhanced gold film and observed the deformation and energy transform in the process. Jia et al. [20] studied the stability of gold/SAM/epoxy resin interfaces with different monolayer chain lengths. In more recent studies, Fang and coworkers utilized a combination of united-atom and all-atom force fields in their MD simulations of nano-indentation on alkanethiol SAMs absorbed on gold substrate [21]. Lane et al. [22] modeled the interaction between water molecules and SAMs and measured the degree of water penetration depending on different initial damage to the SAMs.

All too often, the SAM-modified interfaces are not perfectly flat, and rough SAM surfaces are frequently encountered in real devices [23]. Due to the different nature of the substrate, polishing techniques, and film growth conditions, SAMs exhibit a roughness in RMS ranging from a few to tens of nanometers [24,25], surpassing the chain length of SAM molecules. This roughness profile can significantly affect the formation of SAMs, reduce the real contact area of SAM-modified interface and detriment their desired interfacial properties [26–28]. Duan et al. [29] varied SAM-substrate surface roughness via different etching time and studied its effect on water contact angles. Kulinich et al. [30] calculated the wetting characteristics of various SAM groups and found that surface roughness can lead to considerably increased hydrophobicity of surface. Ulman et al. [31] used surface force apparatus (SFA) to measure the deformation and contact forces of smooth mica and SAMs absorbed to rough gold. Their study found that the pull-off force to separate the two surfaces was dependent on measured roughness of the interface. Xu et al. [24] investigated the adhesion force of Octadecyltriethoxysilane (OTE) SAMs on surface of crystalline Si(100) and silica nano-particle films with atomic force microscopy (AFM). Their experiment indicates that adhesion measured on OTE-modified Si(100) surfaces was approximately 15 times greater than that on the silica particle surfaces, where the latter exhibit rougher profiles in terms of RMS of the height distribution.

This paper is motivated by the recent work of Awasthi et al. [32], where MD simulations were performed on perfectly flat interfaces consisting of a thin gold film and various functionalized SAMs. MD simulations consistently predicted interfacial strengths of Au–SAM interfaces about 50 times higher than those measured by spallation experiments. When probed by atomic force microscopy (AFM), surface roughness measurements of interacting surfaces were found to be about 1 nm, the same order of magnitude as the range of atomistic interactions. Using a continuum model of the interface between a rigid film and substrate, it was shown that nano-scale surface roughness significantly mitigates interfacial interactions and hence that the influence of surface roughness must be correctly incorporated to predict nano-scale interfacial strength. In this work, we study the characteristics of deformation of a thin film on a SAM-modified substrate using a deformable continuum model of the film. Special treatment is given to simulating the spallation process, evaluating the energy exchange and assessing the effective cohesive characteristics of the SAM-enhanced interface.

The article is organized as follows: In Section 2, a brief overview of the MD simulations and experimental observations is provided for completeness. In Section 3, we discuss the deformation of the thin film and its initial profile after it is transfer-printed onto the SAM-enhanced substrate. In Section 4, we focus on the spallation process and evaluate the effective cohesive properties of the film/substrate interface.

2. MD modeling and experimental observations

We begin by summarizing the key results of the MD simulations and the AFM observations which motivate the present work. Fig. 1(a) depicts a schematic of the system composed of a silicon substrate which tethers a layer of SAM about 1 nm in thickness. A thin transfer-printed film of gold rests on the SAM surface directly interacting with the functionalized end of the SAM. As shown in Fig. 1(a), SAMs can be functionalized differently by replacing the head groups. MD simulations were set up for two SAMs with head groups, –CH3 and –SH as shown in Fig. 1(a). These SAMs are respectively called dodecyltriethoxysilane (DTES) and mercapto-undecyltrimethoxysilane (MUTMS). The force-displacement responses of the SAM-Au interfaces of these two cases are shown in Fig. 1(b) and (c), respectively, for different velocities of separation. Note the typical shape of the force-displacement profile first increases with separation, reaches a maximum and then reduces to zero for large interfacial separations. Since MUTMS bonds much stronger with Au than DTES, its interfacial strength is calculated to be about 3 GPa while that of the DTES interface is about 0.9 GPa. Spallation experiments [32,33] for the same interfaces have determined these strengths to be about 80 MPa and 20 MPa, respectively. Though MD simulations yield very similar strength ratio, between MUTMS and DETS, the magnitude of strength is about 50 times higher than those observed experimentally. AFM measurements were performed to probe surface roughness of the top surface of SAM and underside of Au layer (Fig. 1(d)). It was found that the nanoscale surface roughness is about the same order of magnitude as the range of atomistic interactions, i.e., about 1 nm. Spallation test performed on interface with different roughness have determined the interface stress of Au film on the MUTMS-functionalized silicon substrate to be 250% greater than on MUTMS-functionalized fused silica substrates, where the former have a significantly reduced surface roughness (Fig. 1(d)). This might explain the high strength values predicted by MD simulations, which pertain to a perfect interface as shown in insets of Fig. 1(b) and (c). For more details, please refer to references [32,33].

Motivated by experiments and MD simulation results, we investigate the role played by the surface roughness on the spallation strength of SAM-enhanced interfaces. Our model is based on a two-step approach: In the first step (Section 3), the initial equilibrium profile of the deformable gold film transfer-printed on the rough substrate is analyzed, with the interface interaction captured using the cohesive law derived from aforementioned MD simulations. In the second step (Section 4), we use the initial profile obtained in the first step to assess the effective cohesive response associated with a rapid spallation of the gold film.
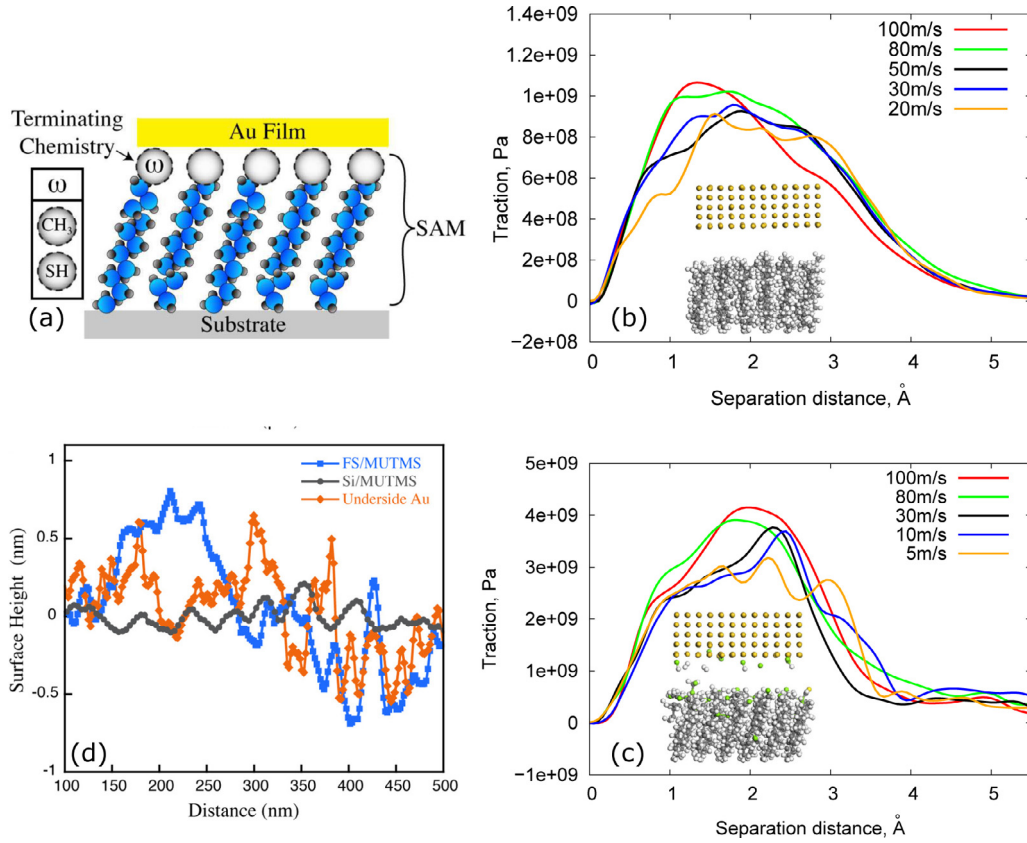
Fig. 1. (a) Schematic of substrate/SAM/Au film system. (b) and (c) MD simulations of separation at the interfaces of DTES/Au and MUTMS/Au film, respectively. As shown in the inset of (b), the weak bonds between the methyl head group and the gold film lead to a clean separation, while the covalent bonds between the sulfur in MUTMS and the gold film leads to the failure of some of the internal chains. The traction-separation curves for different levels of separation velocities imparted to the gold film for DTES/Au and MUTMS/Au systems are shown as well. (d) AFM scan of the Si/MUTMS, Fused Silica(FS)/MUTMS systems and the underside of Au film. This figure is reproduced with permission from [32,33], copyright 2014 American Chemical Society.

3. Initial profile

3.1. Formulation

A 1-D classical 'beam' model is adopted to mimic the behavior of the thin film as it rests over a much stiffer SAM-enhanced substrate. In this model, the SAM-enhanced substrate is taken as a non-deformable solid. In the undeformed state, the film is assumed to be flat. The initial distance $\delta_i(x)$ between a point x along the initially flat film and the rigid rough substrate is given by

$$\delta_i(x) = A\left(1 - \cos\frac{2\pi x}{L}\right), \tag{1}$$

with A denoting the amplitude and L the wavelength of the roughness. After undergoing deformation due to strong cohesive interactions with the substrate, the film deforms. Due to its stiffness, the transfer-printed film does not completely follow the shape of the underlying profile, but rather adopts an equilibrium configuration shown in Fig. 2. For the SAM-enhanced thin film systems of interest (Fig. 1(d)), $A \sim 1$ nm and $L \sim 500$ nm [33]. Adopting the exponential cohesive model given in [34], we express the cohesive traction-separation response along the interface as

$$T_a(x) = \sigma_c \frac{\delta_i(x) + w(x)}{\delta_c} \exp\left[1 - \frac{\delta_i(x) + w(x)}{\delta_c}\right], \tag{2}$$

where the critical displacement, δ_c and the failure strength, σ_c, are obtained from MD simulations, $\delta_i(x)$ is defined by (1) and $w(x)$ is the transverse displacement of the film which needs to be solved. The cohesive relation in (2) is used to describe the interface interaction

in non-contact regions where the cohesive interaction is an attractive force. To incorporate the compressive behavior between the film and the substrate, a linear contact penalty under compression is adopted, which is expressed as

$$T_c(x) = K_n \frac{\sigma_c}{\delta_c}\left[\delta_i(x) + w(x)\right], \tag{3}$$

where K_n is the penalty constant. In this study, we take $K_n = 300$, which suffice to ensure convergence of the compressive force [35,36].
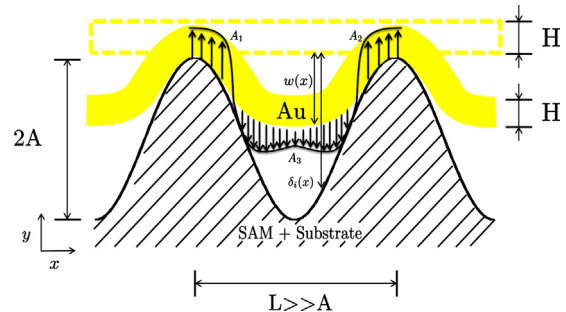

Fig. 2. Schematic of a deformable film (yellow) that rests on roughness of a nanoscale interface (shaded), at equilibrium. $\delta_i(x)$ and $w(x)$ are the initial distance and film displacement at a point x along the length of the film, respectively. A_3 (A_1 and A_2) denotes the portion of the rough interface where attractive (compressive) cohesive tractions apply. (For interpretation of the references to color in this figure legend, the reader is referred to the web version of the article.)

The initial deformation of the film is governed by [37]

$$\frac{EI}{1-v^2}\frac{d^4w(x)}{dx^4} = -T(x), \tag{4}$$

where E, v, I are the Young's modulus, Poisson's ratio and moment of inertia per unit width of the film, respectively. The cohesive traction $T(x)$ is defined by (2) and (3) in non-contact and contact regions, respectively. Periodic boundary conditions dictate $w(0) = w(L)$, $w'(0) = 0$, $w'(L) = 0$. At the same time, the overall equilibrium of the film is expressed by

$$\int_0^L T(x)dx = \int_0^L [T_a(x) + T_c(x)]dx = 0. \tag{5}$$

Now let us introduce non-dimensional parameters $\tilde{x} = \frac{x}{L}$, $\eta = \frac{A}{\delta_c}$, $\lambda = \frac{L}{\delta_c}$, $\tilde{w} = \frac{w}{A}$, and $\beta = \frac{EH^3\delta_c}{12\sigma_c eL^4(1-v^2)}$, with $e = \exp(1)$. With these parameters, the non-dimensional form of the equilibrium equation (4) can be written as

$$\beta\frac{d^4\tilde{w}}{d\tilde{x}^4} = \begin{cases} -(1-\cos 2\pi\tilde{x} - \tilde{w})\exp[\eta(\tilde{w}-1-\cos 2\pi\tilde{x})], & (1-\cos 2\pi\tilde{x} - \tilde{w}) \geq 0 \\ -\dfrac{K_n}{e}(1-\cos 2\pi\tilde{x} - \tilde{w}), & (1-\cos 2\pi\tilde{x} - \tilde{w}) < 0 \end{cases} \tag{6}$$

while the boundary conditions take the form

$$\begin{cases} \tilde{w}(0) = \tilde{w}(1), \\ \tilde{w}\prime(0) = 0, \\ \tilde{w}\prime(1) = 0, \\ \tilde{w}\prime\prime(0) = \tilde{w}\prime\prime(1). \end{cases} \tag{7}$$

The last condition in (7) results from overall equilibrium of the film described by (5).

We observe from (6) that the solution is governed by two non-dimensional parameters, β and η, which characterize the film-substrate system: η accounts for the amplitude of the substrate roughness, while β incorporates the bending stiffness of the film, the properties of the interface, as well as the wavelength of the substrate profile.

3.2. Results

As the film deforms under cohesive interactions with the rough substrate, bending energy is stored in the film [38]. The non-dimensional bending energy ($\tilde{E}_b$) can be expressed as the ratio of the energy (E_b) stored in the film after deformation, to the total cohesive energy (E_c) of a flat interface, and is given as

$$\tilde{E}_b = \frac{E_b}{E_c} = \frac{\beta\eta^2}{2}\int_0^1 \left(\frac{d^2\tilde{w}}{d\tilde{x}^2}\right)^2 d\tilde{x}, \tag{8}$$

where $E_c = e\sigma_c\delta_c L$ is the cohesive energy of a perfectly flat interface over one wavelength L.

Fig. 3 shows the variation of $\tilde{E}_b$ with β for a fixed surface roughness $\eta = 5$, together with deformed profiles at six specific β values labeled A to F. The bending energy ratio curve starts at $\beta = 0$, which corresponds to a perfectly flat interface with no bending energy stored in the film. As β increases owing to an increase of the film thickness or a decrease of the substrate wavelength, the bending energy ratio rises, reaches a maximum (in excess of 60% of the cohesive energy) and undergoes a slight decrease (point B). In this regime, the film remains closely adhered to the substrate (profiles A and B).

Further increasing β from B to E leads to a sharp drop in bending energy as the film snaps from a position closely adhered to the substrate to a quasi-unloaded configuration (profile E). Beyond this critical value of β, the bending energy ratio (from point E to point F) approaches the fully unloaded profile as expected for very stiff films and/or very short wavelength substrates.

The abrupt change of bending energy ratio and the deformed profile at the critical value of β is further described with the solid curve (B→C→D→E) shown in Fig. 3 and obtained using the arc-length method. The actual evolution of bending energy ratio $\tilde{E}_b$ and the deformed profiles with β for this portion shows the smooth but unstable transition between points B and E.

The dependence of $\tilde{E}_b$ on β for different values of η is presented in Fig. 4. Once again, all curves start at $\tilde{E}_b = 0$, since $\beta = 0$ corresponds to a perfectly flat interface, where no bending energy is stored in the film. As β increases, the bending energy increases, reaches a maximum and eventually decays to zero for high values of β i.e., for high film stiffness or short roughness wavelength. For higher roughness ($\eta > 3$), the transition is abrupt due to the aforementioned instability. For smaller η, the β-dependence of $\tilde{E}_b$ is smooth. This result is consistent with predictions made earlier using a surface energy exchange model [38] and that pertaining to the rough surface indenter problem [39].
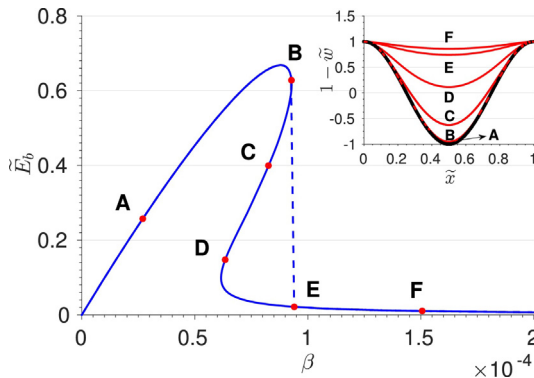

Fig. 3. Bending energy ratio $\tilde{E}_b$ defined in (8) and deformed profiles for the case $\eta = 5$. In the top right figure, A, B, E, and F are deformed film profiles for four values of β denoted in the main figure. An abrupt drop of bending energy ratio occurs from B to E, together with a change of deformed profile. The equilibrium path A→B→C→D→E→F is the actual curve of bending energy ratio $\tilde{E}_b$ and deformed profiles, with C and D corresponding to two unstable equilibrium configurations.
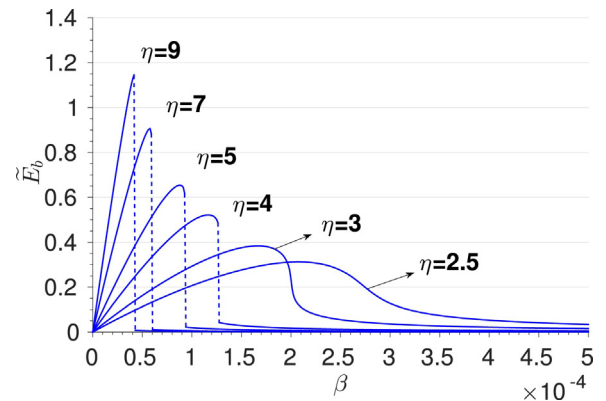

Fig. 4. Effect of β on the bending energy ratio of different values of η. As η increases, the response is increasingly unstable and leads to higher values of stored bending energy.
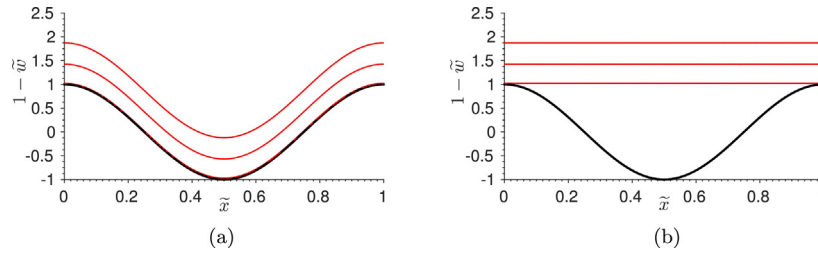
Fig. 5. Schematic of the spallation models: (a) Spallation of the deformed initial configuration found in Section 3. (b) Spallation of a perfectly rigid film. During spallation, the film is assumed to be lifted rigidly from the substrate.

4. Spallation

Once the initial deformed shape of the transfer-printed thin film is obtained, it is used to study the spallation process. The film is assumed to be rigid since spallation occurs too rapidly for the film to further deform before it is spalled from the substrate [33,40].

Fig. 5(a) demonstrates this spallation process of a film with an initially deformed profile. As the film uniformly moves away from the substrate, no deformation incurs until the film is fully spalled and the cohesive interaction between the film and substrate vanishes. As a reference, Fig. 5(b) shows the spallation of a film under perfectly rigid assumption, which states that the bending stiffness of the film is so large that there is no film deformation under cohesive tractions. In the rigid case, the interaction between the film and the substrate can be fully determined by using (1), (2) and (3).

4.1. Formulation

The effective cohesive traction $\overline{T}(\tilde{\delta})$ can be calculated as the average traction on the film using the non-dimensional parameters introduced in the previous section:

$$\overline{T}(\tilde{\delta}) = \frac{1}{L} \int_0^L [T_a(x) + T_c(x)] dx = \sigma_c \int_0^1 [\tilde{\delta} + \eta(\tilde{w} + 1 - \cos 2\pi\tilde{x})]$$
$$\times \exp[1 - \tilde{\delta} - \eta(\tilde{w} + 1 - \cos 2\pi\tilde{x})] d\tilde{x}, \tag{9}$$

where $\tilde{\delta} = \frac{\delta}{\delta_c}$ denotes the non-dimensional uniform displacement of the film. The effective cohesive energy, obtained by calculating the area under the effective cohesive curve, can be written as

$$\tilde{E}_c = \frac{L}{E_c} \int_0^\infty \overline{T}(\tilde{\delta}) d\tilde{\delta}, \tag{10}$$

where E_c has been defined after (8).

4.2. Results

In addition to the effective cohesive traction of a deformable thin film defined by (9), a closed-form expression for the effective cohesive response of a perfectly rigid film (Fig. 5(b)) denoted by $\overline{T}^R(\delta)$ can be obtained as

$$\overline{T}^R(\tilde{\delta}) = \frac{1}{L} \int_0^L T^R(x, \tilde{\delta}, \eta) dx = \sigma_c[(\tilde{\delta} + \eta)I_0(\eta) - \eta I_1(\eta)]e^{1 - \tilde{\delta} - \eta}, \tag{11}$$

with I_0 and I_1 denoting the modified Bessel function of the first kind. In this case, the effective cohesive curve does not depend on β but only on η, implying that, the effective cohesive response is only related to the substrate profile amplitudes when the bending stiffness of the thin film is very large. The resulting effective cohesive curves of a perfectly rigid film for different values of η are presented in Fig. 6. It is worth noting that the effective traction on the perfectly rigid film at $\tilde{\delta} = 0$ is not zero. This is a direct result
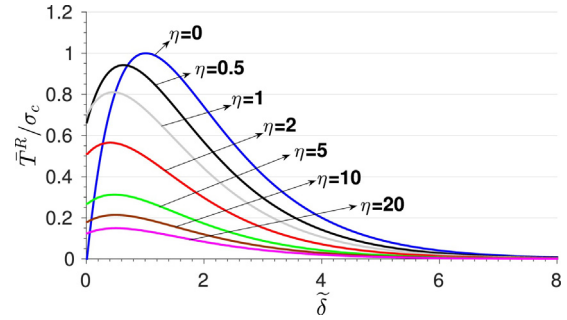

Fig. 6. Effective traction-separation curves for different values of η under the perfectly rigid assumption. When $\eta = 0$, the original cohesive law is retrieved. As the roughness amplitude grows larger (i.e., as η increases), the maximum cohesive traction becomes smaller. Note that, under the rigid film assumption, the cohesive traction on the film at $\tilde{\delta} = 0$ is not zero.

of the rigidity assumption of the film, neglecting the compressive behavior between the film and the substrate.

Fig. 7 shows the effective cohesive response of the deformable film-substrate system for $\eta = 5$ and for four values of β, labeled A, B, E and F, corresponding to the four initial deformed configurations labeled in Fig. 3. The effective cohesive response for a perfectly rigid film and the exponential cohesive law are also presented for comparison. At $\tilde{\delta} = 0$, the film in the deformable case has an average traction $\overline{T} = 0$, which corresponds to the initial equilibrium state. As $\tilde{\delta}$ increases, the film moves away from the substrate and the value of the effective cohesive traction rapidly increases before reaching the maximum. In the configuration where the film has an initial profile closely attached to the substrate, the resulting effective cohesive response (curve A) is very close to the interface cohesive law. At the other end of the spectrum, the effective cohesive strength is substantially smaller (by about 70% for $\beta = 1.5 \times 10^{-4}$) if initially the film is in a quasi-unloaded configuration. The effective cohesive
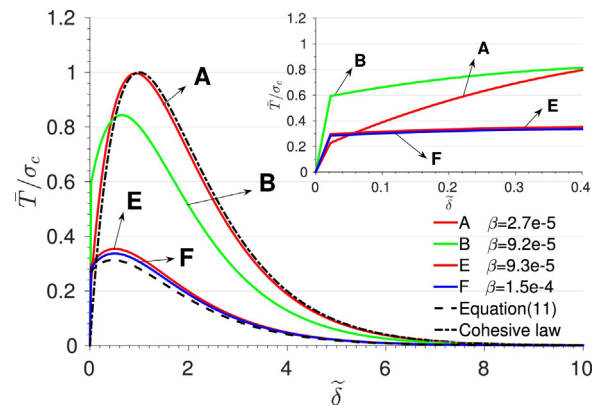

Fig. 7. Effective traction-separation response for $\eta = 5$ with four values of β denoted by A, B, E and F (See Fig. 3). The exponential cohesive laws and the rigid film approximation (11) are also shown for comparison. The inset shows the responses for small values of $\tilde{\delta}$.
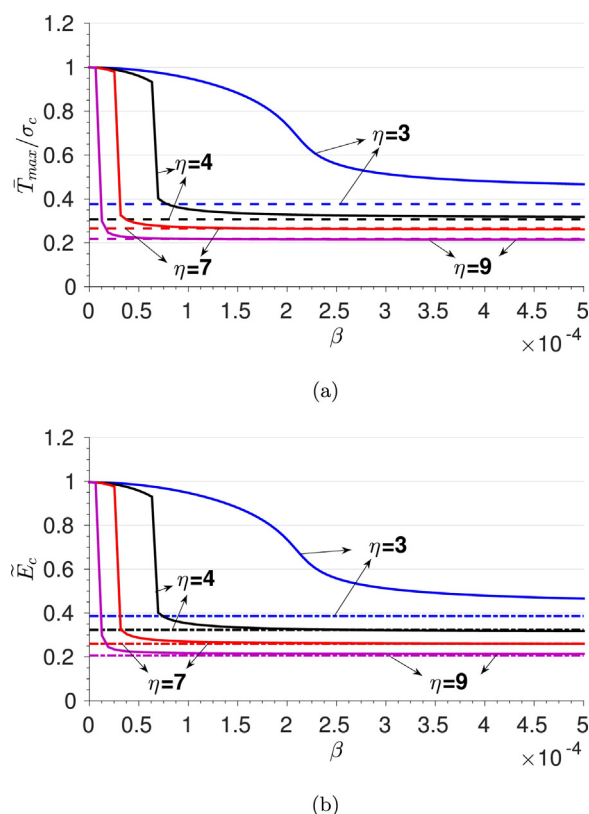
Fig. 8. (a) Maximum effective cohesive traction and (b) effective cohesive energy on the film, for different values of η. When η is small, $\overline{T}_{\max}$ and $\tilde{E}_c$ are smooth. When η is large, $\overline{T}_{\max}$ and $\tilde{E}_c$ show abrupt changes. The result for the perfectly rigid case is presented in dotted line and is the limit of the deformable case as $\beta \to \infty$.

response thus greatly depends on the initial profiles of the thin film. It is worth noting that, when $\tilde{\delta}$ goes from 0 to the first non-zero point, the contact regions of the film becomes non-contact regions. This causes the traction on the film corresponding to the first non-zero $\tilde{\delta}$ to have an abrupt jump instead of a smooth transition from zero, which also leads to a shift of the $\tilde{\delta}$ where maximum effective cohesive traction occurs.

Fig. 8(a) and (b) depict the effective cohesive strength and the effective cohesive energy of the system for different values of η, respectively. The two figures have a similar pattern due to the exponential nature of the effective cohesive interaction. The curves start with $\overline{T}_{\max}/\sigma_c = 1$ and $\tilde{E}_c = 1$ at $\beta = 0$, where the effective interfacial cohesive response is the same as the exponential cohesive model (see Fig. 7). The largest cohesive traction $\overline{T}_{\max}$ and effective cohesive energy $\tilde{E}_c$ then decrease as β increases. At smaller η values, $\overline{T}_{\max}$ and $\tilde{E}_c$ decrease smoothly with β, while at larger η values, $\overline{T}_{\max}$ and $\tilde{E}_c$ reach a critical point and then undergo abrupt drops before decreasing smoothly with β. Note that there is a slight difference in the value of $\tilde{E}_c$ and $\overline{T}_{\max}/\sigma_c$, due to the detachment of the contact region and thus a shift of $\tilde{\delta}$ where the maximum effective traction occurs, as shown in Fig. 7. Comparing Figs. 3 and 8, we observe that the critical β where the drops of $\overline{T}_{\max}$ and $\tilde{E}_c$ occur is the same as the critical β where the drops of $\tilde{E}_b$ and the snaps of initial film profile occur. This further demonstrates that the spallation and effective cohesive behavior of the SAM-modified substrate-film system greatly depend on the characteristics of the initial deformed profile of the thin film.

5. Conclusion

The present work focuses on evaluating the influence of surface roughness on the effective cohesive strength of the interface

between a SAM-enhanced substrate and a transfer-printed thin film of gold. Though MD results of perfectly ordered atomistic surfaces have shown similar qualitative trend as experiments, they over-predict the interfacial cohesive strengths by a factor of about 50. AFM measurements have shown that the roughness of these surfaces is comparable ($\sim$1 nm) to the range of atomistic interactions. We employ a two-step continuum approach to evaluate the effect of roughness: First, the initial profile of a deformable gold film after transfer-printed on the rough substrate is analyzed, using a cohesive law achieved from MD simulations. Second, the initial profile obtained in the first step is used to assess the effective cohesive response associated with rigid spallation of the gold film. We found that the initial profile of the thin film and associated effective cohesive strength of the interface are governed by two non-dimensional parameters which reflect material properties of the film, cohesive nature of the interface and the substrate roughness amplitude and wavelength. The analysis is effective in demonstrating that the incorporation of roughness reduces the cohesive strength of the interface by up to 70%.

Acknowledgements

References

[1] W. Azzam, A. Bashir, A. Terfort, T. Strunskus, C. Wöll, Combined STM and FTIR characterization of terphenylalkanethiol monolayers on Au (111): effect of alkyl chain length and deposition temperature, Langmuir 22 (8) (2006) 3647–3655.

[2] J. Noh, H.S. Kato, M. Kawai, M. Hara, Surface structure and interface dynamics of alkanethiol self-assembled monolayers on Au (111), J. Phys. Chem. B 110 (6) (2006) 2793–2797.

[3] A. Ulman, Formation and structure of self-assembled monolayers, Chem. Rev. 96 (4) (1996) 1533–1554.

[4] M. Schaeferling, S. Schiller, H. Paul, M. Kruschina, P. Pavlickova, M. Meerkamp, C. Giammasi, D. Kambhampati, Application of self-assembly techniques in the design of biocompatible protein microarray surfaces, Electrophoresis 23 (18) (2002) 3097–3105.

[5] M. Mrksich, C.S. Chen, Y. Xia, L.E. Dike, D.E. Ingber, G.M. Whitesides, Controlling cell attachment on contoured surfaces with self-assembled monolayers of alkanethiolates on gold, Proc. Natl. Acad. Sci. U. S. A. 93 (20) (1996) 10775–10778.

[6] M.D. Losego, M.E. Grady, N.R. Sottos, D.G. Cahill, P.V. Braun, Effects of chemical bonding on heat transport across interfaces, Nat. Mater. 11 (6) (2012) 502–506.

[7] Z. Tian, A. Marconnet, G. Chen, Enhancing solid–liquid interface thermal transport using self-assembled monolayers, Appl. Phys. Lett. 106 (21) (2015) 211602.

[8] D.K. Aswal, S. Lenfant, D. Guerin, J.V. Yakhmi, D. Vuillaume, Self assembled monolayers on silicon for molecular electronics, Anal. Chim. Acta 568 (1) (2006) 84–108.

[9] I.H. Campbell, J.D. Kress, R.L. Martin, D.L. Smith, N.N. Barashkov, J.P. Ferraris, Controlling charge injection in organic electronic devices using self-assembled monolayers, Appl. Phys. Lett. 71 (24) (1997) 3528–3530.

[10] B.G. Bush, F.W. Del-Rio, C. Jaye, D.A. Fischer, R.F. Cook, Interfacial mechanical properties of alkylsilane monolayers on silicon substrates, J. Microelectromech. Syst. 22 (1) (2013) 34–43.

[11] J.E. Houston, C.M. Doelling, T.K. Vanderlick, Y. Hu, G. Scoles, I. Wenzl, T.R. Lee, Comparative study of the adhesion, friction, and mechanical properties of CF3-and CH3-terminated alkanethiol monolayers, Langmuir 21 (9) (2005) 3926–3932.

[12] H.I. Kim, J.E. Houston, Separating mechanical and chemical contributions to molecular-level friction, J. Am. Chem. Soc. 122 (48) (2000) 12045–12046.

[13] H.I. Kim, V. Boiadjiev, J.E. Houston, X.Y. Zhu, J.D. Kiely, Tribological properties of self-assembled monolayers on Au, SiOx and Si surfaces, Tribol. Lett. 10 (1–2) (2001) 97–101.

[14] K.M. Liechti, S.R. Na, M. Wakamatsu, O. Seitz, Y. Chabal, A high vacuum fracture facility for molecular interactions, Exp. Mech. 53 (2) (2013) 231–241.

[15] P.F. Li, H. Zhou, X.H. Cheng, Nano/micro tribological behaviors of a self-assembled graphene oxide nanolayer on Ti/titanium alloy substrates, Appl. Surf. Sci. 285 (2013) 937–944.

[16] J.J. Gerdy, W.A. Goodard, Atomistic structure for self-assembled monolayers of alkanethiols on Au (111) surfaces, J. Am. Chem. Soc. 118 (13) (1996) 3233–3236.

[17] L. Zhang, W.A. Goddard, S. Jiang, Molecular simulation study of the c(4 × 2) superlattice structure of alkanethiol self-assembled monolayers on Au (111), J. Chem. Phys. 117 (15) (2002) 7342–7349.

[18] C. Da Wu, T.H. Fang, Y.J. Huang, Effects of non-flat contact and interference on self-assembled monolayers under sliding friction, Appl. Surf. Sci. 257 (9) (2011) 4123–4128.

[19] T.H. Fang, W.J. Chang, Y.C. Fan, C.I. Weng, Molecular dynamics of contact behavior of self-assembled monolayers on gold using nanoindentation, Appl. Surf. Sci. 255 (21) (2009) 8931–8934.

[20] J. Jia, Y.D. Huang, J. Long, J.M. He, H.X. Zhang, Molecular dynamics simulation of the interface between self-assembled monolayers on Au (111) surface and epoxy resin, Appl. Surf. Sci. 255 (13) (2009) 6451–6459.

[21] T. Fang, W. Chang, S. Lin, C. Fang, Interface dynamics and mechanisms of nanoindented alkanethiol self-assembled monolayers using molecular simulations, J. Colloid Interface Sci. 345 (1) (2010) 19–26.

[22] J.M.D. Lane, M. Chandross, C.D. Lorenz, M.J. Stevens, G.S. Grest, Water penetration of damaged self-assembled monolayers, Langmuir 24 (11) (2008) 5734–5739.

[23] R. Maboudian, W.R. Ashurst, C. Carraro, Self-assembled monolayers as anti-stiction coatings for MEMS: characteristics and recent developments, Sens. Actuators A: Phys. 82 (1) (2000) 219–223.

[24] C. Xu, R.L. Jones, J.D. Batteas, Dynamic variations in adhesion of self-assembled monolayers on nanoasperities probed by atomic force microscopy, Scanning 30 (2) (2008) 106–117.

[25] B.G. Bush, F.W. DelRio, J. Opatkiewicz, R. Maboudian, C. Carraro, Effect of formation temperature and roughness on surface potential of octadecyltrichlorosilane self-assembled monolayer on silicon surfaces, J. Phys. Chem. A 111 (49) (2007) 12339–12343.

[26] E.A. Weiss, R.C. Chiechi, G.K. Kaufman, J.K. Kriebel, Z. Li, M. Duati, M.A. Rampi, G.M. Whitesides, Influence of defects on the electrical characteristics of mercury-drop junctions: self-assembled monolayers of n-alkanethiolates on rough and smooth silver, J. Am. Chem. Soc. 129 (14) (2007) 4336–4349.

[27] E.F. Douglass Jr., P.F. Driscoll, D. Liu, N.A. Burnham, C.R. Lambert, W.G. McGimpsey, Effect of electrode roughness on the capacitive behavior of self-assembled monolayers, Anal. Chem. 80 (20) (2008) 7670–7677.

[28] S.D. Moré, H. Graaf, M. Baune, C. Wang, T. Urisu, Influence of substrate roughness on the formation of aliphatic self-assembled monolayers (SAMs) on silicon (100), Jpn. J. Appl. Phys. 41 (6S) (2002) 4390.

[29] Y. Duan, Y. Li, Y. Ding, D. Li, Effect of surface roughness and release layer on anti-adhesion performance of the imprint template, Appl. Surf. Sci. 257 (8) (2011) 3220–3225.

[30] S.A. Kulinich, M. Farzaneh, Alkylsilane self-assembled monolayers: modeling their wetting characteristics, Appl. Surf. Sci. 230 (1) (2004) 232–240.

[31] R.A. Quon, A. Ulman, T.K. Vanderlick, Use of the surface forces apparatus to directly measure the influence of self-assembled monolayers on the adhesion and deformation of rough solids, Langmuir 16 (8) (2000) 3797–3802.

[32] A.P. Awasthi, M.E. Grady, I.H. Kim, N.R. Sottos, P.H. Geubelle, Nanoscale mechanical tailoring of interfaces using self-assembled monolayers, Mech. Mater. 98 (2016) 71–80.

[33] M.E. Grady, P.H. Geubelle, P.V. Braun, N.R. Sottos, Molecular tailoring of interfacial failure, Langmuir 30 (37) (2014) 11096–11102.

[34] X.P. Xu, A. Needleman, Numerical simulations of fast crack growth in brittle solids, J. Mech. Phys. Solids 42 (9) (1994) 1397–1434.

[35] M.P. O'day, P. Nath, W.A. Curtin, Thin film delamination: a discrete dislocation analysis, J. Mech. Phys. Solids 54 (10) (2006) 2214–2234.

[36] V. Tvergaard, Cohesive zone representations of failure between elastic or rigid solids and ductile solids, Eng. Fract. Mech. 70 (14) (2003) 1859–1868.

[37] R.W. Soutas-Little, Elasticity, Courier Corporation, 1999.

[38] G. Carbone, P. Decuzzi, Elastic beam over an adhesive wavy foundation, J. Appl. Phys. 95 (8) (2004) 4476–4482.

[39] P.R. Guduru, Detachment of a rigid solid from an elastic wavy surface: theory, J. Mech. Phys. Solids 55 (3) (2007) 445–472.

[40] J. Wang, R.L. Weaver, N.R. Sottos, A parametric study of laser induced thin film spallation, Exp. Mech. 42 (1) (2002) 74–83.